Optics Letters

Extreme ultraviolet broadband imaging spectrometer using dispersion-matched zone plates

Yahia Mostafa,[1,2] Zoi Bouza,[1,2] James Byers,[3] Ievgeniia Babenko,[1,4] Wim Ubachs,[1,2] Oscar O. Versolato,[1,2] and Muharrem Bayraktar[3,*]

[1]Advanced Research Center for Nanolithography, Science Park 106, 1098 XG Amsterdam, The Netherlands
[2]Department of Physics and Astronomy, and LaserLaB, Vrije Universiteit Amsterdam, De Boelelaan 1081, 1081 HV Amsterdam, The Netherlands
[3]Industrial Focus Group XUV Optics, MESA+ Institute for Nanotechnology, University of Twente, Drienerlolaan 5, 7522 NB Enschede, The Netherlands
[4]V.N. Karazin Kharkiv National University, 4 Svobody Sq., Kharkiv 61022, Ukraine
*m.bayraktar@utwente.nl

Received 5 June 2023; accepted 12 July 2023; posted 17 July 2023; published 9 August 2023

We present simultaneous 1D imaging and broadband spectroscopy of a laser-produced plasma (LPP) source of extreme ultraviolet light, using a tapered zone plate that is matched to the dispersion of a transmission grating. We describe the design and fabrication of the zone plates in the 5–80 nm wavelength regime with designed spatial resolution of ∼10 μm and spectral resolution of ∼0.8 nm. Subsequently, we benchmark the imaging spectrometer with a solid tin target LPP. Plane wave propagation simulations qualitatively match the experimental results and confirm the device performance.

https://doi.org/10.1364/OL.496995

The reliability, throughput, and efficiency of extreme ultraviolet (EUV) lithography machines depend on the characteristics of the EUV light source, which is currently a laser-produced plasma (LPP) generated from microdroplets of tin [1–4]. This tin LPP emits light from the soft x ray to the visible region, with its emission peaking in the 13.5 nm ± 1% "in-band" region where multilayer mirrors (MLMs) can be employed to guide the light [5]. Maximizing in-band emission compared with the complementary out-of-band emission improves the quality of the EUV source [6,7]. Out-of-band EUV light contributes to collector mirror heating and ionization of ambient hydrogen gas which can damage nearby optics. Additionally, out-of-band light cannot be reflected by the narrow-bandwidth multilayer mirror (MLM) optical systems employed in EUV lithography and contributes to power loss [5,8]. Longer-wavelength, deep ultraviolet emissions may still be reflected by the MLMs and expose the wafer, potentially reducing the pattern contrast [9,10]. Accordingly, it is critical to investigate the emissions in the out-of-band region.

Two fundamental techniques for characterizing plasma sources are spectroscopy and imaging. The spectrum of a microdroplet tin LPP in a 5.5–265.5-nm wavelength range was previously studied [5]. However, this emission spectrum represents the spatial average across the plasma and does not provide information on the spatial distribution of the emission. This distribution is key for understanding the further transport of light through the complex optics system. Understanding the spatial distribution provides the means for optimizing source brightness in the EUV regime while obtaining information on the emission area in the (deep) ultraviolet wavelength band enables an assessment of how much of the light falls within the etendue—and would potentially contribute to wafer exposure. Spatial information of the emission can be obtained using, e.g., pinhole or concave mirror imaging since refractive elements are not applicable due to the high absorption of EUV light. Concave mirror imaging however relies on wavelength-dependent reflections limiting the numerical aperture (NA) and is particularly alignment sensitive. The more accessible technique of pinhole imaging is typically limited in resolution given the minimum available distances to the plasma, leading to a low NA. For 1D imaging, the pinhole may be changed to a slit to increase transmission.

Generally, when combining imaging with wavelength selectivity, established imaging techniques are restricted to either very broad wavelengths (e.g., pinhole imaging combined with a metallic filter) or very narrow bandwidths (e.g., imaging using MLMs). Fresnel zone plate (ZP) optics provide an alternative method of focusing EUV light [11–13], enabling a combination of relatively high NA and long working distances. ZPs can be accurately fabricated using nano-fabrication techniques, and have been successfully applied as high-resolution focusing lenses for arbitrary, single wavelengths of light ranging from the soft x ray to UV region [12,14,15]. However, Fresnel ZPs are highly chromatic. As a result, only a narrow wavelength band can be imaged from light emitted by a broadband plasma source, with the other wavelengths being out of focus.

We present an imaging spectrometer operating across a broad 5–80-nm range with a spectral resolution of ∼0.8 nm (at 13.5 nm), combined with a designed spatial resolution of ∼10 μm. This novel device employs a transmission grating in series with a set of one-dimensional zone plates that are individually matched, or *tapered*, to a particular wavelength according to the grating dispersion. We note that the concept of Fresnel zone tapering was introduced previously, but for optimizing

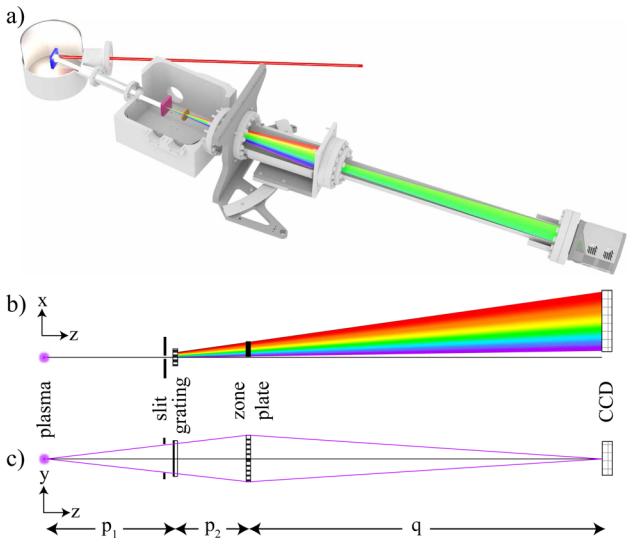

Fig. 1. (a) Schematic 3D overview of the experimental setup, (b) top-down view showing the spectrometer axis (x), and (c) side view showing the imaging axis (y).

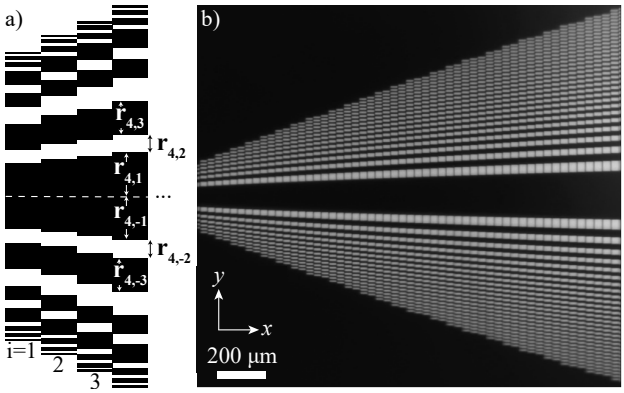

Fig. 2. Dispersion-matched zone plate design. (a) A schematic of the design where index i indicates the zone plate number in the dispersion axis. The radius $r_{i,n}$ of the nth zone of the ith zone plate is given in the text. (b) Optical microscopy image of the tapered zone plate designed for the range 5–80 nm.

single- and not for multi-wavelength operation [16–18]. Our imaging spectrometer is designed for one-dimensional imaging of plasma light sources in the extreme, vacuum, and deep ultraviolet regimes.

Figure 1(a) shows a 3D schematic view of the setup, demonstrating the laser impacting a solid tin target, along with the operation of the imaging spectrometer. In Figs. 1(b) and 1(c), we show the diffraction axis and the imaging axis, respectively. At a distance $p_1 = 53$ cm, a 150-µm slit is used in combination with a 780-lines/mm transmission diffraction grating to disperse the light. The diffracted light impacts a set of 1D wavelength-tapered zone plates at a distance $p_2 = 5$ cm from the diffraction grating. The zone plates image the source onto a back-illuminated Greateyes (GE2048 512BI UV1) CCD at a distance $q = 110$ cm. This combination of distances results in a magnification $M = 1.9$.

We show the design of the zone plate in Fig. 2(a). Along the diffraction axis, a series of 1D zone plates are constructed, with each individual zone plate matching a specific wavelength as dispersed by the grating. The radius $r_{i,n}$ of the nth zone of the ith zone plate, dispersion-matched to the λ_i wavelength, is determined by

$$r_{i,n} = \sqrt{n\lambda_i\left(f + \frac{n\lambda_i}{4}\right)} \quad \text{with} \quad \lambda_i = d\frac{x_i}{\sqrt{p_2^2 + x_i^2}}, \tag{1}$$

where f is the focal distance, d is the grating period of 1.3 µm (corresponding to the 780-l/mm grating), and p_2 and q are as previously described. The spatial resolution of the imaged source is determined by $\Delta w = \lambda f/2r_N$. To maintain near-diffraction-limited performance, the magnitude of the focus shift Δf due to the finite wavelength resolution $\Delta\lambda$ (being 0.8 nm at 13.5 nm for the used grating [19]) should be less than the depth of focus (DOF) of the system. This sets a limit on the useful number of zones of the ZP given by $N \leq \lambda/\Delta\lambda$. Any zones beyond this number do not improve the spatial resolution. In the following, the number of zones N at each wavelength λ_i is set to achieve a constant spatial resolution across all wavelengths, $\Delta w \equiv 10$ µm. We note that the design choices are highly interwoven, with a higher resolution grating enabling higher spatial resolution in step with wavelength resolution (given the capabilities to produce zone widths below 2 µm, a spatial resolution better than 3 µm would be achievable in principle). However, higher-resolution gratings would reduce the spectral window provided for a single CCD position and the current design presents a trade-off between sufficient magnification, range, and resolution taking into account limitations for the current implementation.

The fabrication process of the ZPs is similar to processes that have been previously described [19,20]. The ZP stack consists of Si_3N_4 (200 nm), Cr (15 nm), Au (200 nm), and Cr (15 nm) layers to act as fully absorbing layers to produce an amplitude ZP. Patterns are defined by optical lithography, combined with lift-off and etching. The Si wafer is etched from the backside, enabling free-standing structures. To keep the integrity of the absorber zones, periodic vertical support bars are implemented in the design of the system. The width of the support bars is 4 µm with a period of 40 µm. For practical purposes, we use the support bar period as the width corresponding to the spectral resolution $\Delta\lambda$. The effect of any support bars on the measured spectra can be neglected.

A 1-mm-thick poly-crystalline tin target is mounted onto a 2D translation stage in a vacuum chamber held at 10^{-6} mbar. Using an Nd:YAG 1-µm laser, we irradiate the tin target at 10 Hz while regularly moving the stage to irradiate a new spot. The laser beam has a temporal FWHM of 6 ns and a spatial FWHM of 60 µm. We set the laser power density to $1.6 \times 10^{11}\ W/cm^2$ for the measurements shown in this work (cf. Ref. [21]). The imaging spectrometer described in this work is mounted at 30° backward with respect to the laser beam propagation as shown in Fig. 1(a). First, we only install the transmission grating and exclude the zone plates to obtain the emission spectrum as shown in Fig. 3(a). It covers the 5–25-nm wavelength range captured at a single CCD position. In all data presented here and in the following, a background subtraction has been performed. The CCD image is summed vertically to produce the spectrum shown in the lower segment of the plot. The resulting spectrum is similar to previously obtained spectra for solid and liquid tin LPPs with its main emission feature at 13.5 nm resulting from transitions between multiple excited states in multiple charged tin ions [5–7,22].

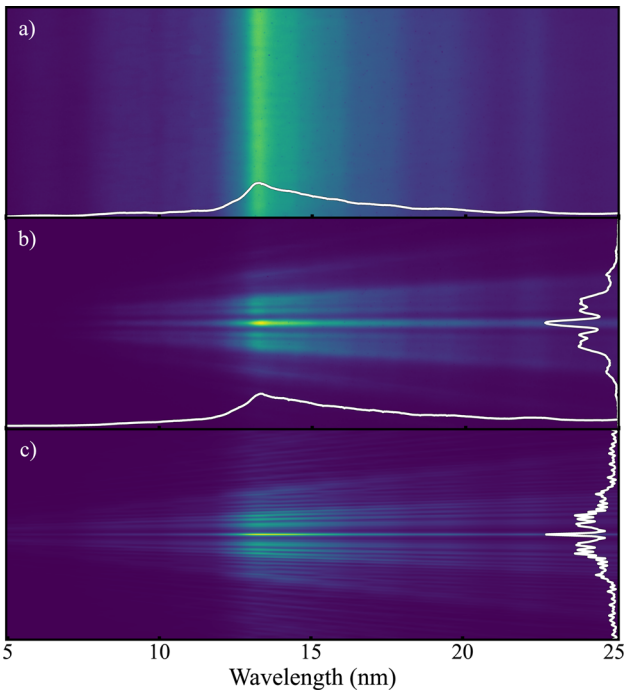

Fig. 3. Experimental and simulation results of tin LPP generated light traversing dispersion-matched zone plates and grating in the 5–25-nm regime. (a) Experimentally acquired spectrum from LPP (see main text) without ZP system with the binned spectrum shown as a lineout. (b) Experimentally acquired spectroscopic image. The bottom lineout represents the spectrum as averaged across the first-order (center) image. The right lineout represents the image at 13.5 nm. (c) Simulations of the dispersion matched zone plate system. The right lineout represents the image at 13.5 nm.

By adding the dispersion-matched zone plate, the wavelength-dependent source image is obtained, as shown in Fig. 3(b). The figure exhibits a central band alongside several diverging features that are the result of the various diffraction orders of the zone plate. It is the central band, originating from the first diffraction order, that represents the 1D source image. The diverging band are the result of zeroth-, third-, and fifth-order diffraction (even diffraction orders are suppressed [19]). A vertical lineout at $\lambda = 13.5$ nm is shown on the right side of the plot; the spectrum (summed over the central band) is inset on the bottom for comparison.

To better understand the obtained image, we next execute wave propagation simulations to verify the imaging response of the ZPs, following the angular spectrum method outlined in Ref. [23]. We adopt a simplified scheme and for each wavelength, simulate the diffraction of a monochromatic plane wave through its corresponding set of zones. The simulation is repeated for the third and fifth *grating* diffraction orders (i.e., any particular set of zones is impinged on by wavelengths having 1/3 and 1/5 of the value of the corresponding first order). The resulting intensity profile at the focal distance is scaled by the experimentally measured spectrum, summed for all orders weighed by the inverse square of the order, as shown in Fig. 3(c) [24]. A vertical lineout across the center of the propagated images (at the focal plane) is taken and aggregated for all wavelengths. The simulation results are convoluted with a 2D Gaussian function to account for the finite spectral resolution (set to $2\Delta\lambda$=1.6 nm at 13.5 nm along the dispersive axis) which in turn causes image blurring (approximately 8 μm) given that a single zone is impinged on by a wavelength band. The lineout for $\lambda = 13.5$ nm is shown on the right, to be compared to the experimental lineout in Fig. 3(b).

We observe good qualitative agreement between simulation and experiment. The main differences can be attributed directly to the fact that the LPP has finite size and the obtained image thus gives direct insight into the spatial emission characteristics. By varying the CCD position laterally, along the dispersive x axis, we can study the plasma emission for longer wavelengths. The CCD is moved in steps corresponding to the width of the CCD chip while maintaining some overlap between subsequent positions. In Fig. 4(a), four such images are stitched by moving the CCD a total of 4° toward the laser axis, corresponding to the wavelength range 5–80 nm. Similar to Fig. 3(b), the spectrum is obtained along the first-order image and shown in the lower segment of the plot as a lineout. In Fig. 4(b), we show the spectrum-normalized result to remove intensity variation along the x axis due to underlying spectral variations and highlight the presence of the first-order image across all wavelengths. We note that some noisy features at the edges of the image, due to low signal levels, and non-perfect stitching features are also visible. Care should be taken in interpreting the source size in these images. Higher diffraction orders of the grating affect the

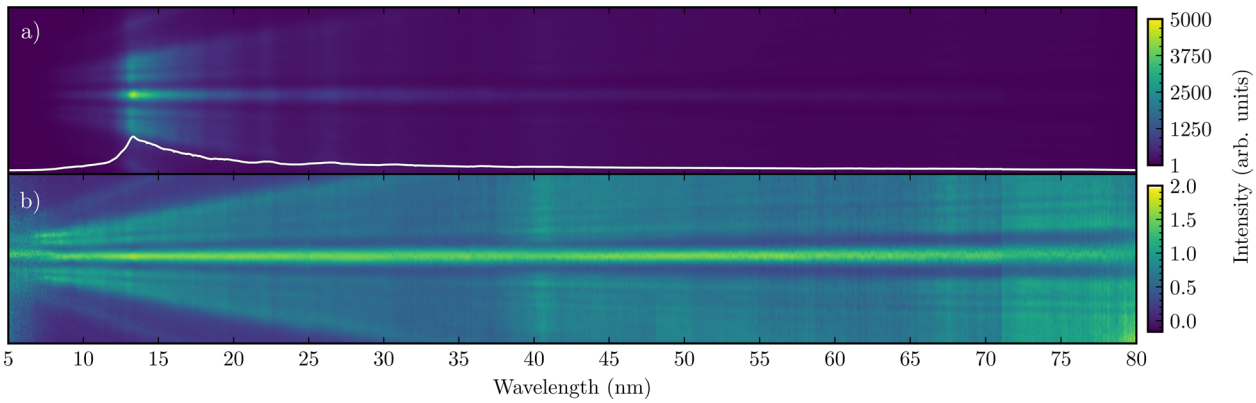

Fig. 4. Experimental results of dispersion-matched tapered zone plates and grating in the 5–80-nm regime. The total image is a composite of exposures at subsequent CCD positions along x. (a) Emission spectrum of solid tin target LPP in linear color scale, highlighting the prominence of the 13.5-nm emission feature. The image center is binned vertically and shown at the bottom as a lineout. (b) Spectrum-normalized result, highlighting the central image across all wavelengths and the higher grating diffraction orders of 13.5 nm (third order at 40.5 nm and fifth order at 67.5 nm).

observed image. The zone-plate's nth diffraction order of an mth grating diffraction order will coincide with the first orders on the CCD for $n = m$ (since the focal distance $f_n = r_1^2/n\lambda_m$). The prominent higher orders are that of the 13.5-nm peak observed at 40.5 nm and 67.5 nm in Fig. 4(b). Contributions of higher orders to the image however are noticeable only at odd orders of the main emission feature at 13.5 nm and do not impede interpretation of the overall spatial emission characteristics. In specific applications, filters and zone blocks may be added to suppress higher orders if need be, and the concept may be straightforwardly extended to other wavelengths (shorter and longer).

Returning to the dominant first-order image, we note that its width increases with wavelength, indicating an increasing source size with wavelength. This observation is in line with the expectation that when emission from a hot surface is considered, the temperature reduces moving away from the core. The center of the plasma is the smallest and hottest region of the plasma, responsible for the emission of the shortest wavelengths, as these are emitted by the higher charges states. Longer wavelengths are expected to be emitted from areas away from the core where the temperature is also lower.

In conclusion, we demonstrate an effective spectrally resolved imaging device for wavelengths in the range 5–80 nm. Using a combination of a transmissive diffraction grating and a sequence of zone plates matched to the diffraction, simultaneous measurement of the emission spectrum and 1D imaging is achieved. We employ the described device to study laser-produced plasma light sources. The results are supported by wave propagation simulations of the zone plate. Having demonstrated the working principle in proof-of-concept experiments, the imaging spectrometer may find application in plasma characterization studies in the nanolithography field and beyond, e.g., in research on short-wavelength light sources.

Funding. Topconsortium voor Kennis en Innovatie (SUN); Rijksdienst voor Ondernemend Nederland; European Research Council (Starting 802648); Nederlandse Organisatie voor Wetenschappelijk Onderzoek (VIDI 15697).

Acknowledgments. We would like to thank Henk-Jan Boluijt, Dr. Laurens van Buuren, and Caspar Bruineman for their contribution to the design and the construction of the experimental setup, Dr. Boris Vratzov for the fabrication of the zone plates and gratings, and Dr. Mengqi Du for valuable contribution to the simulations part of this work.

Disclosures. The authors declare no conflicts of interest.

Data availability. Data underlying the results presented in this paper are not publicly available at this time but may be obtained from the authors upon reasonable request.

REFERENCES

1. O. O. Versolato, Plasma Sources Sci. Technol. **28**, 083001 (2019).
2. V. Y. Banine, K. N. Koshelev, and G. H. P. M. Swinkels, J. Phys. D: Appl. Phys. **44**, 253001 (2011).
3. M. Purvis, I. V. Fomenkov, A. A. Schafgans, M. Vargas, S. Rich, Y. Tao, S. I. Rokitski, M. Mulder, E. Buurman, M. Kats, J. Stewart, A. D. LaForge, C. Rajyaguru, G. Vaschenko, A. I. Ershov, R. J. Rafac, M. Abraham, D. C. Brandt, and D. J. Brown, Proc. SPIE **10583**, 1058327 (2018).
4. H. Mizoguchi, H. Nakarai, T. Abe, K. M. Nowak, Y. Kawasuji, H. Tanaka, Y. Watanabe, T. Hori, T. Kodama, Y. Shiraishi, T. Yanagida, G. Soumagne, T. Yamada, T. Yamazaki, and T. Saitou, in *2018 China Semiconductor Technology International Conference (CSTIC)* (2018), pp. 1–7.
5. Z. Bouza, J. Byers, J. Scheers, R. Schupp, Y. Mostafa, L. Behnke, Z. Mazzotta, J. Sheil, W. Ubachs, R. Hoekstra, M. Bayraktar, and O. O. Versolato, AIP Adv. **11**, 125003 (2021).
6. F. Torretti, A. Windberger, A. Ryabtsev, S. Dobrodey, H. Bekker, W. Ubachs, R. Hoekstra, E. V. Kahl, J. C. Berengut, J. R. C. López-Urrutia, and O. O. Versolato, Phys. Rev. A **95**, 042503 (2017).
7. J. Scheers, C. Shah, A. Ryabtsev, H. Bekker, F. Torretti, J. Sheil, D. A. Czapski, J. C. Berengut, W. Ubachs, J. R. C. López-Urrutia, R. Hoekstra, and O. O. Versolato, Phys. Rev. A **101**, 062511 (2020).
8. R. M. van der Horst, J. Beckers, E. A. Osorio, D. I. Astakhov, W. J. Goedheer, C. J. Lee, V. V. Ivanov, V. M. Krivtsum, K. N. Koshelev, D. V. Lopaev, F. Bijkerk, and V. Y. Banine, J. Phys. D: Appl. Phys. **49**, 145203 (2016).
9. K. Liu, Y. Li, F. Zhang, and M. Fan, Jpn. J. Appl. Phys. **46**, 6568 (2007).
10. G. Yang and Y. Li, Proc. SPIE **8322**, 83222V (2012).
11. F. Döring, B. Rösner, M. Langer, A. Kubec, A. Kleibert, J. Raabe, C. A. F. Vaz, M. Lebugle, and C. David, Optica **7**, 1007 (2020).
12. J. O. Schunck, F. Döring, B. Rösner, J. Buck, R. Y. Engel, P. S. Miedema, S. K. Mahatha, M. Hoesch, A. Petraru, H. Kohlstedt, C. Schüssler-Langeheine, K. Rossnagel, C. David, and M. Beye, Optica **8**, 156 (2021).
13. A. V. Baez, J. Opt. Soc. Am. **51**, 405 (1961).
14. F. Marschall, Z. Yin, J. Rehanek, M. Beye, F. Döring, K. Kubiček, D. Raiser, S. T. Veedu, J. Buck, A. Rothkirch, B. Rösner, V. A. Guzenko, J. Viefhaus, C. David, and S. Techert, Sci. Rep. **7**, 8849 (2017).
15. A. Jonas, T. Meurer, B. KanngieSSer, and I. Mantouvalou, Rev. Sci. Instruments **89**, 026108 (2018).
16. S. Ali and C. Jacobsen, J. Opt. Soc. Am. A **37**, 374 (2020).
17. L. E. Ocola, J. Maser, S. Vogt, B. Lai, R. Divan, and G. B. Stephenson, Proc. SPIE **5539**, 165 (2004).
18. K. Li and C. Jacobsen, J. Synchrotron Radiat. **25**, 1048 (2018).
19. S. J. Goh, H. M. J. Bastiaens, B. Vratzov, Q. Huang, F. Bijkerk, and K. J. Boller, Opt. Express **23**, 4421 (2015).
20. M. Bayraktar, H. M. J. Bastiaens, C. Bruineman, B. Vratzov, and F. Bijkerk, NEVAC Blad **54**, 14 (2016).
21. R. Schupp, F. Torretti, R. Meijer, M. Bayraktar, J. Scheers, D. Kurilovich, A. Bayerle, K. Eikema, S. Witte, W. Ubachs, R. Hoekstra, and O. Versolato, Phys. Rev. Appl. **12**, 014010 (2019).
22. L. Behnke, R. Schupp, Z. Bouza, M. Bayraktar, Z. Mazzotta, R. Meijer, J. Sheil, S. Witte, W. Ubachs, R. Hoekstra, and O. O. Versolato, Opt. Express **29**, 4475 (2021).
23. K. Matsushima and T. Shimobaba, Opt. Express **17**, 19662 (2009).
24. H. W. Schnopper, L. P. V. Speybroeck, J. P. Delvaille, A. Epstein, E. Källne, R. Z. Bachrach, J. Dijkstra, and L. Lantward, Appl. Opt. **16**, 1088 (1977).